POLYOXOMETALATES

Open Access
RESEARCH ARTICLE

Self-assembled vesicles containing podophyllotoxin covalently modified with polyoxometalates for antitumor therapy

Lingmei Li[1,§], Yixiang Song[2,§], Jinyu Liu[1], Quanfu Wang[1], Jiacheng Wu[1], Xiaochuan Lu[1], Dejin Zang[1] ✉, and Teng Liu[1] ✉

[1] *School of Pharmaceutical Sciences & Institute of Materia Medica, Shandong First Medical University & Shandong Academy of Medical Sciences, State Key Laboratory of Advanced Drug Delivery and Release Systems, Key Laboratory for Biotechnology Drugs of National Health Commission (Shandong Academy of Medical Sciences), Key Lab for Rare & Uncommon Diseases of Shandong Province, Jinan 250117, China*
[2] *Department of Pediatric Oncology, Shandong Cancer Hospital and Institute, Shandong First Medical University and Shandong Academy of Medical Sciences, Jinan 250117, China*
[§] *Lingmei Li and Yixiang Song contributed eqully to this work.*

Cite This: *Polyoxometalates*, **2025**, *4*, 9140085

Read Online

ABSTRACT: Several polyoxometalates (POMs) have been shown to possess antitumor activity. In this study, hydrophilic POMs were combined with the hydrophobic drug podophyllotoxin (PPT) to create an amphiphilic anti-cancer drug PPT-POM-PPT, which can self-assemble into hollow vesicles. The properties of these vesicles, such as the critical aggregation concentration, were characterized. These vesicles had low hemolytic activity and high stability. Cytotoxicity tests showed that the PTT-POM-PPT vesicles exhibit strong antitumor activity against lung and liver cancer cells without significantly affecting normal cells. Cell uptake experiments confirm that the PPT-POM-PPT vesicles can easily penetrate cell membranes and effectively enter tumor cells, thus exerting anti-tumor effects. Furthermore, these vesicles co-localized with lysosomes. Moreover, these PPT-POM-PPT vesicles exhibit synergistic effects of PPT and POMs. They are efficient drug delivery platforms that act as both the carrier and the active drug, avoiding the potential risks associated with additional carrier ingredients. In summary, due to their anticancer properties, POMs and PPT facilitate the generation of novel amphiphilic self-assembling vesicles, providing a theoretical basis and enabling clinical applications of POMs in cancer therapy.

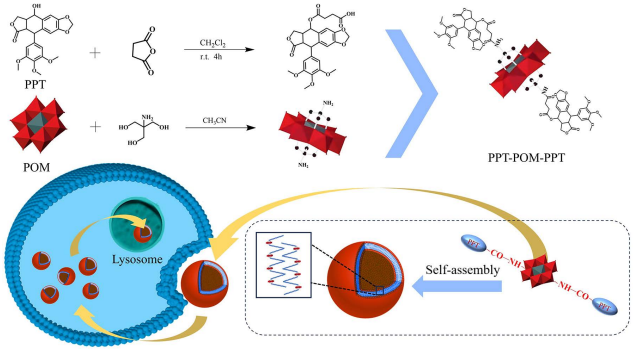

KEYWORDS: polyoxometalates, podophyllotoxin, self-assembly, vesicles, anti-tumor

1 Introduction

Polyoxometalates (POMs) comprise inorganic metal-oxygen clusters that are formed when oxygen atoms connect with various pre-transition metals, such as Mo, W, V, Nb, and Ta [1]. POMs are multifunctional materials that have potential applications in many fields, including catalysis, environmental science, and medicine [2–4]. Recent studies have shown that POMs possess potent anticancer properties, making them promising therapeutic candidates [5]. Due to their unique structures, they can effectively inhibit various tumor types [6–8]. Although the specific mechanism by which POMs induce apoptosis in cancer cells is unclear, existing studies suggest that it may trigger intracellular oxidative stress by generating reactive oxygen species (ROS), creating a hypoxic environment and ultimately leading to cell death [9–11]. POMs have several advantages over traditional drugs, including high surface reactivity, abundant active centers, excellent catalytic efficiency, and strong adsorption capacity [12–14]. Due to these unique properties, POMs are attractive candidates for developing novel metal-based anticancer drugs.

Inorganic POMs are being increasingly researched as antitumor drugs due to their affordability and good water solubility. However, their poor lipid solubility limits their cell membrane permeability [15]. Furthermore, while small organic anticancer molecules often exhibit moderate inhibitory concentrations at the nanomolar level, higher concentrations of POMs are required to exert anti-proliferative effects [16, 17]. Modifying POMs by introducing hydrophobic organic groups via covalent bonds is an innovative strategy to overcome these limitations [18–20]. These POM-organic hybrids are structurally well-defined and can trigger synergistic effects, imparting the materials with new functional properties and performance advantages [21–23]. A study showed that the anti-tumor effects of amantadine-modified POMs against human breast

Received: September 27, 2024; **Revised:** December 23, 2024
Accepted: February 8, 2025

✉Address correspondence to Dejin Zang, zangdejin_lm@163.com; Teng Liu, liuteng@sdfmu.edu.cn

https://doi.org/10.26599/POM.2025.9140085

cancer cells MCF-7 [24] were higher than those of unmodified POMs and amantadine alone. These POMs significantly inhibited cell proliferation at 100 μg·mL^{-1}, and the degree of inhibition increased with an increase in the POM concentration. The antitumor activity of cyclopentadienyl titanium-modified POMs has also been elucidated [25]. Experiments using *in vivo* models created by introducing liver cancer cells SSMC-7721, leukemia cells HL-60, and colon cancer cells HLC into rats by single subcutaneous inoculation revealed that the modified POMs significantly reduced the tumor burden of the experimental rats. Dehydrocholic acid-modified POMs exhibited potent cytotoxicity in experiments targeting breast cancer cells while showing lower toxicity toward non-cancerous breast epithelial cells [26]. Therefore, besides enhancing the antitumor activity and selectivity of POMs, these modifications improve their ability to target tumor cells precisely. Furthermore, modification with organic compounds effectively enhanced the lipid solubility and optimized the cell membrane penetration ability of POMs, improving their anticancer activity and bioavailability.

In the organic group-modified POM complexes, POMs are the hydrophilic components that synergistically interact with the hydrophobic organic groups and enhance their amphiphilicity [27–29]. These structurally diverse complexes enable the in-depth understanding of the aggregate behavior of amphiphilic organic group-modified POMs formed in solution [30–32]. Amphiphilic POM-cholic acid hybrid materials have been shown to spontaneously assemble into vesicles in a mixed solvent system of methanol/toluene [33]. This self-assembly process is mainly driven by the van der Waals forces between the cholic acid groups and the electrostatic forces between the POM clusters, promoting the formation of stable vesicles. These vesicles were also prepared using POM-organoalkoxysilane hybrids [34]. Because of their amphiphilic properties, these vesicles can easily enter or bind to the surface of membranes, enhancing membrane fluidity and promoting cell penetration and uptake. However, these studies mainly focused on the self-assembly or anti-tumor properties of POMs. The potential applicability of POMs combined with anti-cancer drugs to form vesicles has not been elucidated yet.

Several studies have explored the modification of POMs with the organic groups of antitumor drugs as a promising therapeutic strategy. In this study, the anti-tumor drug podophyllotoxin (PPT) was modified with POMs to create an amphiphilic drug PPT-POM-PPT, which was shown to self-assemble into vesicles (Fig. 1). Furthermore, the size, critical aggregation concentration (CAC), and stability of these vesicles were characterized. The inhibitory effect of the PPT-POM-PPT vesicles was investigated using lung cancer cells (H1299 and A549), human liver cancer cells (HepG-2), and human embryonic kidney cells (HEK293). Chemical modifications of POMs with anti-tumor drugs enable the effective regulation of their biological properties, strengthening their drug activity. It also overcomes the limitation of POMs due to poor lipid solubility and potential toxicity. Therefore, this system combines the dual anti-tumor advantages of PPT and POMs, achieving stronger inhibitory effects. Its unique self-assembling ability leads to the spontaneous formation of vesicles, making it an efficient drug delivery system. In addition to avoiding any risks that may be introduced by external carriers, it ensures the high efficiency and precision of drug delivery. Therefore, these POM drugs have broad prospects as potential therapeutic agents for several diseases.

2 Experimental section

2.1 Materials

$(TBA)_4[\alpha\text{-}Mo_8O_{26}]$ was synthesized as described previously [35]. $Mn(CH_3COO)_3{\cdot}2H_2O$, tris(hydroxymethyl) aminomethane (TRIS), succinic anhydride, and 2-ethoxy-1-ethoxycarbonyl-1,2-dihydroquinoline (EEDQ) were purchased from Aladdin Reagent (China) and used as received. Fluorescein isothiocyanate (FITC) and methylthiazoletetrazolium (MTT) were obtained from Sigma-Aldrich Co. All other reagents and solvents were purchased from Sinopharm Chemical Reagent (China) and used without purification.

2.2 Synthesis and characterization of PPT-POM-PPT

2.2.1 *Synthesis of the amino-modified POMs*

$(TBA)_4[\alpha\text{-}Mo_8O_{26}]$ (1 g), $Mn(CH_3COO)_3{\cdot}2H_2O$ (0.19 g), and TRIS (0.2 g) were mixed in acetonitrile for 16 h under reflux heating. After cooling down the reaction system to room temperature, the insoluble sediment was removed by filtration [36] and an orange-colored POM ($(TBA)_3(MnMo_6O_{18}[(OCH_2)_3CNH_2]_2)$) was obtained after washing with cold acetonitrile and cold ether, filtration, and vacuum drying.

2.2.2 *Synthesis of the carboxyl-modified PPT*

After dissolving PPT (1 g) in anhydrous dichloromethane, 4-dimethylaminopyridine (0.33 g), triethylamine (0.27 g), and succinic anhydride (0.72 g) were added to this mixture. The reaction was performed at room temperature for 4 h and was monitored using thin-layer chromatography (TLC) [37, 38]. At the end of the reaction, the solution was diluted with 100 mL of dichloromethane and washed thrice with 0.1 mol·L^{-1} hydrochloric acid solution. The organic phase was first dried with anhydrous

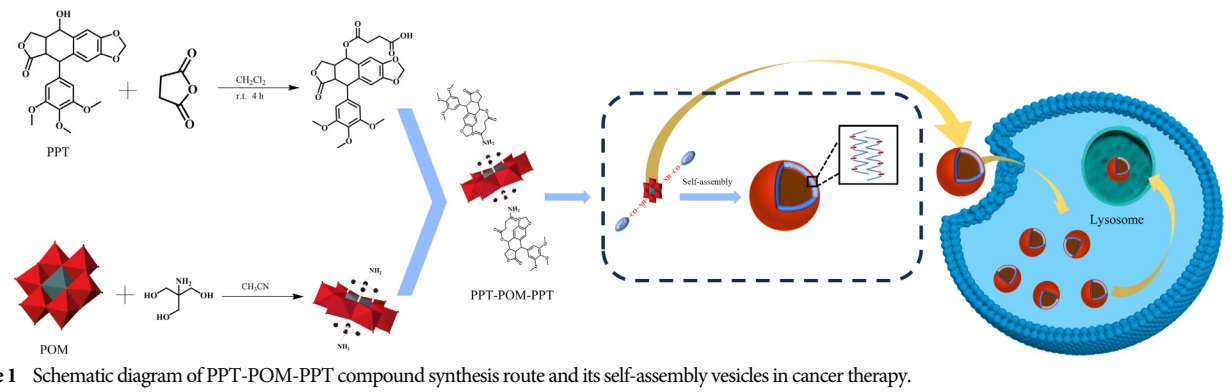

Figure 1 Schematic diagram of PPT-POM-PPT compound synthesis route and its self-assembly vesicles in cancer therapy.

sodium sulfate. Then, dichloromethane was removed under reduced pressure and vacuum-dried to obtain a white powder PPT-COOH.

2.2.3 Synthesis of PPT-POM-PPT

EEDQ (0.29 g) was dissolved in anhydrous acetonitrile under nitrogen. Then, PPT-COOH (0.32 g) was added, and the reaction was warmed to reflux for 30 min. Then, POMs (0.5 g) were added to the reaction solution, and the reaction was refluxed for 20 h. At the end of the reaction, the solution was cooled to room temperature, concentrated by rotary evaporation, and then dropped into ethyl acetate under stirring. After precipitation, the reaction was filtered, dissolved in a small amount of acetonitrile, and precipitated in an ether atmosphere to obtain PPT-POM-PPT ($(TBA)_3(MnMo_6O_{18}[(OCH_2)_3CNHCOC_{25}H_{25}O_9]_2)$).

2.2.4 Structural characterization

PPT-POM-PPT was characterized via nuclear magnetic resonance spectroscopy (^{1}H NMR) using the Bruker Avance 800 MHz spectrometer with DMSO-d_6 as the solvent. Fourier transform infrared spectroscopy (FTIR) spectra were obtained on a Perkin Elmer Spectrum 65 spectrometer equipped with a DTGS detector (32 scans) at a resolution of 4 cm^{-1} in a KBr pellet. The ultraviolet–visible (UV–vis) spectra of PPT-POM-PPT were obtained using the Shimadzu UV-2600 spectrophotometer. Thermal gravimetric (TG) measurements were performed on a Q500 Thermal Analyzer (Mettler Toledo) in flowing N_2 with a heating rate of 10 °C·min^{-1}. X-ray diffraction (XRD) data were collected using the D8 Advance diffractometer (Bruker, Germany) equipped with a Cu-Kα radiation source and a graphite monochromator. X-ray photoelectron spectroscopy (XPS) data were collected using the EscaLab 250Xi equipped with a monochromatized Al Kα X-ray source (1486.71 eV).

2.3 Preparation and characterization of the vesicles

The PPT-POM-PPT vesicles were prepared using the dialysis method. Briefly, 1 mg of PPT-POM-PPT was accurately weighed and dissolved in 0.5 mL acetonitrile. Then, it was slowly dropped into a mixed solvent of 4.5 mL acetonitrile and water at a 1:1 ratio (v/v). The compound was transferred to a dialysis bag and dialyzed for 72 h to obtain the PPT-POM-PPT vesicle solution. The prepared vesicles were used as stock solutions. A series of solutions with gradient concentrations can be configured.

Determining the CAC: The conductivity of the PPT-POM-PPT solution was measured as a function of the concentration at five different temperatures using a low-frequency conductivity analyzer. To ensure the reliability of the outcomes, triplicate measurements were performed at each temperature. The steady-state fluorescence spectrum was obtained using the Hitachi F-7000 fluorescence spectrophotometer at five different temperatures (25, 30, 35, 40, and 45 °C). The concentration of pyrene, used as the fluorescent probe, was kept constant throughout the experiment. The excitation wavelength was 335 nm. The excitation and emission slits were set to 2.5 and 10 nm, respectively. The spectrum between 360 and 550 nm was obtained at a scan rate of 1200 nm·min^{-1}. The temperature was controlled using a thermostatic water tank (accuracy 0.1 °C). All other experiments were conducted at room temperature.

2.4 Methods to test the stability of the vesicles

Evaluating the time stability of the vesicles: PPT-POM-PPT (200 μg·mL^{-1}) was kept at 4 °C and taken out at intervals of 1, 5, 15, and 30 days, respectively. The size and distribution of the vesicles were measured with a Zetasizer instrument (Malvern Nano ZS Zetasizer). The scanning times were set to 3, and the detection temperature was set to 25 °C.

Evaluating the dilution stability of the vesicles: PPT-POM-PPT vesicles obtained by dialysis were diluted by 0, 10, 100, 250, 500, and 1000 times, respectively. The sizes and size distributions of the vesicles in these solutions were measured with a Zetasizer instrument to examine whether the vesicles could maintain structural stability under different dilutions.

Evaluating the lyophilized solubility of the vesicles: After dialysis, 8 mL of the PPT-POM-PPT vesicle solution was divided into two parts. One part was mixed thoroughly with 0.2 g (5%) mannitol and placed in a freeze-drying oven. After approximately 2 h of pre-freezing and vacuum drying for 12 h, a white and fluffy freeze-dried powder was obtained. This powder was added to 4 mL of deionized water for re-dissolution. The size of the vesicles was determined after redissolving them to assess whether vesicles can be formed after lyophilization and to compare the effect of lyophilization with and without the lyophilized protective agent (mannitol).

2.5 Hemolysis assay

Blood samples collected from mice were diluted with an equal volume of saline and centrifuged (4 °C, 1000 r·min^{-1}, 10 min) to obtain the pellet containing red blood cells (RBCs). The concentrated RBCs were washed thrice and resuspended in phosphate buffered saline (PBS, pH 7.4) to get a 2% (v/v) erythrocyte suspension. To each centrifuge tube, 1 mL of 2% RBC suspension was added, followed by 3 mL of PPT-POM-PPT vesicles at concentrations ranging from 5–200 μg·mL^{-1}. Water and PBS (pH 7.4) were used as positive and negative controls, representing maximum and minimum hemolysis, respectively. All tests were performed in triplicate. After incubation at 37 °C for 4 h, the experimental and control groups were centrifuged (4 °C, 3000 r·min^{-1}, 10 min), and the absorbance values at 578 nm of the supernatants were determined using a microplate spectrophotometer.

2.6 Cytotoxicity assay

For the MTT assay, H1299, A549, HepG-2, and HEK293 cells (1×10^4 cells/well) were plated in Dulbecco's modified Eagle's medium (DMEM) with 10% fetal bovine serum in 96-well plates for 24 h. Then, these cells were treated with the desired concentrations (20, 40, 60, 100, and 200 μg·mL^{-1}) of free PPT, POMs, and PPT-POM-PPT vesicles and cultured for 24 and 48 h. The medium in each well was replaced with fresh medium containing MTT. After 4 h of incubation, the tetrazolium salts were metabolized to formazan crystals and the medium was removed. DMSO was added to each well and shaken gently to dissolve the precipitates. The absorbance of each well at 490 nm was determined using a microplate spectrophotometer.

2.7 Cell apoptosis

The early and late apoptosis of cells induced by the PPT-POM-PPT vesicles were assessed using flow cytometry (FCM). A549 cells (1×10^4 cells/well) were plated in six-well plates and incubated for 24 h. Then, the cells were stained with Annexin-V and propidium iodide. An untreated group was used as the control.

2.8 Cellular uptake and co-localization

Cellular uptake and co-localization of the vesicles were observed

using confocal laser scanning microscopy (CLSM). Cells (1×10^4 cells/well) were seeded in six-well plates and cultured for 24 h. Then, the medium in each well was replaced by fresh medium containing FITC-labeled PPT-POM-PPT vesicles. After incubation for 8 h, the cells were rinsed with PBS and fixed with 4% paraformaldehyde. The uptake of cells treated with 100 μg·mL^{-1} of FITC-labeled PPT-POM-PPT vesicles for 1, 3, 6, and 12 h was analyzed using the ImageJ software.

To study the co-localization of the FITC-labeled PPT-POM-PPT vesicles, A549 cells were incubated with Lyso-Tracker Red. The cell uptake was detected qualitatively using CLSM. The excitation wavelengths of FITC and Lyso-Tracker Red were 488 and 543 nm, respectively.

3 Results and discussion

3.1 Characterization of PPT-POM-PPT

The ^{1}H NMR spectrum of the prepared PPT-POM-PPT revealed peak ratios at the TBA signal (from 0.8 to 1.7, 1.9, and 3.2 ppm) and the TRIS CH_2 signal (around 64 ppm), validating the structure of the PPT-POM-PPT. The signals at 5.89–7.00 ppm were assigned to the phenyl groups of PPT. In addition to showing the successful synthesis of PPT-POM-PPT, the ^{1}H NMR results demonstrated that the POMs maintained their structural integrity before and after the reaction (Fig. 2(a)). The ^{1}H NMR spectra of PPT and POMs are shown in Figs. S1 and S2 in the Electronic Supplementary Material (ESM). The characteristic peaks associated with PPT and POMs have been marked on the figures, highlighting the unique chemical signatures.

The characteristic stretching and vibrating bands were correctly localized in the FTIR spectra (Fig. 2(b)). The characteristic peak at 664 cm^{-1} belonged to the vibration of the Mo–O–Mo group, while those at 940 and 918 cm^{-1} represented the terminal Mo=O units. The other reference bands associated with the TBA residues were located around 2900 cm^{-1}. The C–H stretch of the methyl group was located at 2934 cm^{-1}. The bend of the methyl group was located at 1380 cm^{-1} [39]. The FTIR spectrum of PPT-POM-PPT showed a characteristic peak at around 1735 cm^{-1} from the ester bond. The peaks at 3291, 1669, 1542, and 1253 cm^{-1} indicate N–H stretching, C=O stretching, N–H bending, and C–N stretching vibrations, respectively. These results also demonstrated the introduction of PPT into PPT-POM-PPT.

Due to the charge transfer transition of the $p_\pi(O_t) \rightarrow d_{\pi^*}(Mo)$ ligand to the metal in the POMs, an absorption peak and a shoulder peak were obtained at approximately 210 and 240 nm, respectively [40]. Using acetonitrile as the solvent and blank background, the UV absorption spectrum of the POMs was obtained by scanning between 200 and 400 nm. The strongest absorption and shoulder peaks were obtained at 215 and 240 nm, respectively, consistent with previous studies (Fig. 2(c)).

In the TG curves of POMs, PPT and PPT-POM-PPT displayed one major weight loss stage from 30 to 600 °C (Fig. 2(d)). The POM curve showed weight loss values mainly due to the loss of

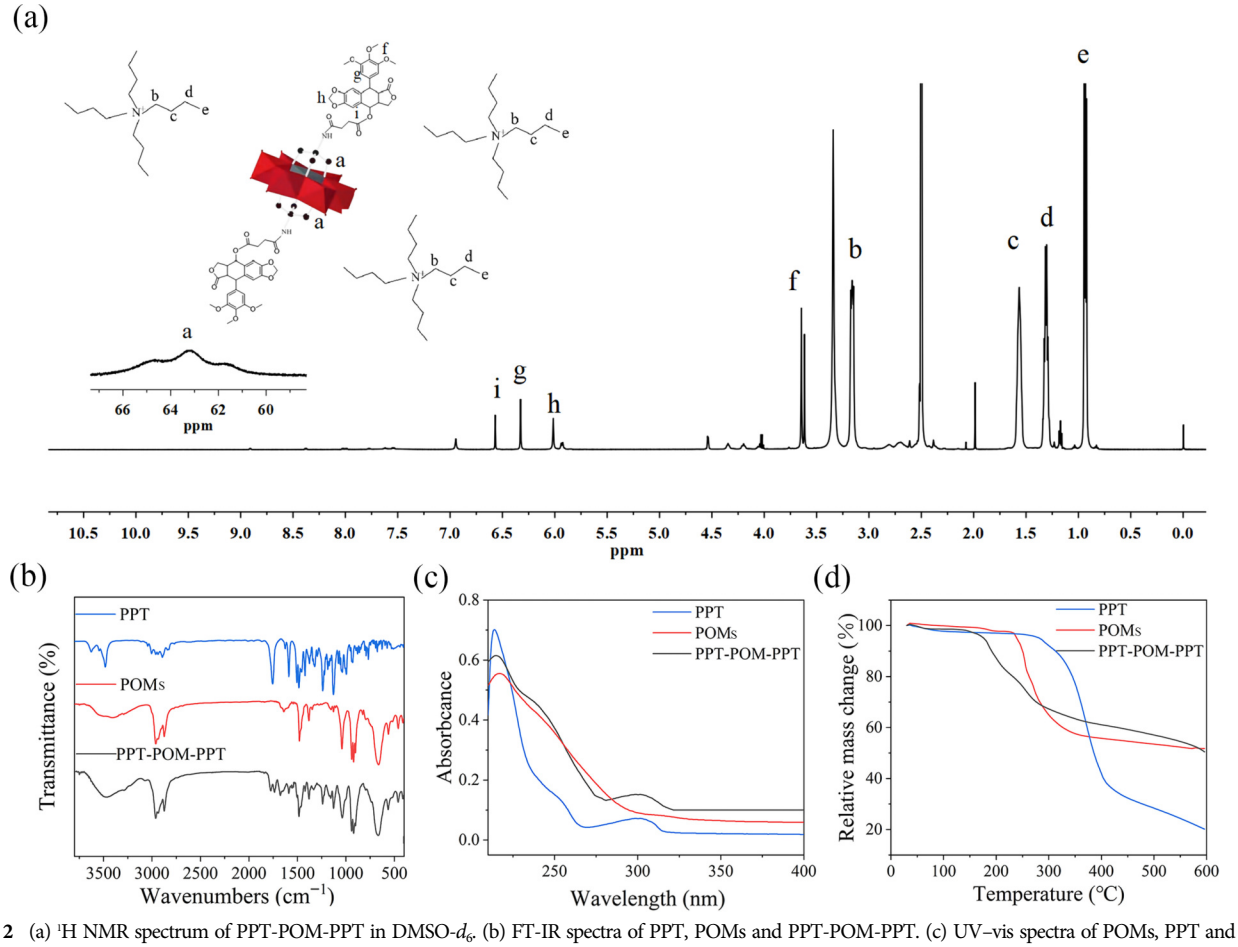

Figure 2 (a) ^{1}H NMR spectrum of PPT-POM-PPT in DMSO-d_6. (b) FT-IR spectra of PPT, POMs and PPT-POM-PPT. (c) UV–vis spectra of POMs, PPT and PPT-POM-PPT. (d) TG curves of POMs, PPT and PPT-POM-PPT.

water molecules and the decomposition of organic ligands [41]. At approximately 190 °C, the PPT-POM-PPT curve showed a significant weight loss, probably due to the dissociation of the POMs from PPT. As the temperature increased, the weight loss became more pronounced. When the temperature reached 300 °C, the rate of weight loss slowed down and was very close to the proportion of POMs, indicating that most of the PPT was lost from PPT-POM-PPT. The electrospray ionization mass spectrometry (EMI-MS) spectra of POMs and PPT-POM-PPT are shown in Figs. S3 and S4 in the ESM. The molecular weight of POMs is 1881 Da and the molecular weight of PPT-POM-PPT is 2633 Da. Because TBA in the molecular structure is prone to fracture during ionization, the complete molecular weight is not shown.

The crystallinity and structure of all samples were tested by X-ray powder diffraction (Fig. 3). The simulated XRD results of the POMs were fitted with the crystallographic information file CCDC-189392 provided by the Cambridge Crystallographic Data Center (CCDC) as the initial model using the Mercury software [36]. As shown in Fig. 3(a), the simulated and experimental XRD patterns of the POMs have similar characteristic diffraction peaks, indicating that the structure of POMs is maintained. The curves for POMs had several peaks at 2θ of 8°–9° and 11°–12°, which were characteristic of an Anderson-type polyoxometalate structure [42]. The XRD results showed that the diffraction peaks of PPT and POMs were not simply superimposed but wide and weak, indicating that the interaction of PPT and the POM polyanion led to the amorphous shape of the POMs and reduced crystallinity.

XPS spectroscopy analysis of the elemental composition and chemical states of the POMs and PPT-POM-PPT (Fig. 3(b)) confirmed the presence of Mo, Mn, C, and O elements, which are the skeleton components of POMs and PPT-POM-PPT. In the C 1s spectrum of POMs, the peaks at 285.29, 284.59, and 284.16 eV corresponded to the C–O, C–N, and C–C bonds, respectively. Similarly, the peaks in PPT-POM-PPT were very close in value to these. Likewise, the Mn 2p spectra for both POMs and PPT-POM-PPT matched the characteristic peaks indicative of Mn^{2+}. The XPS

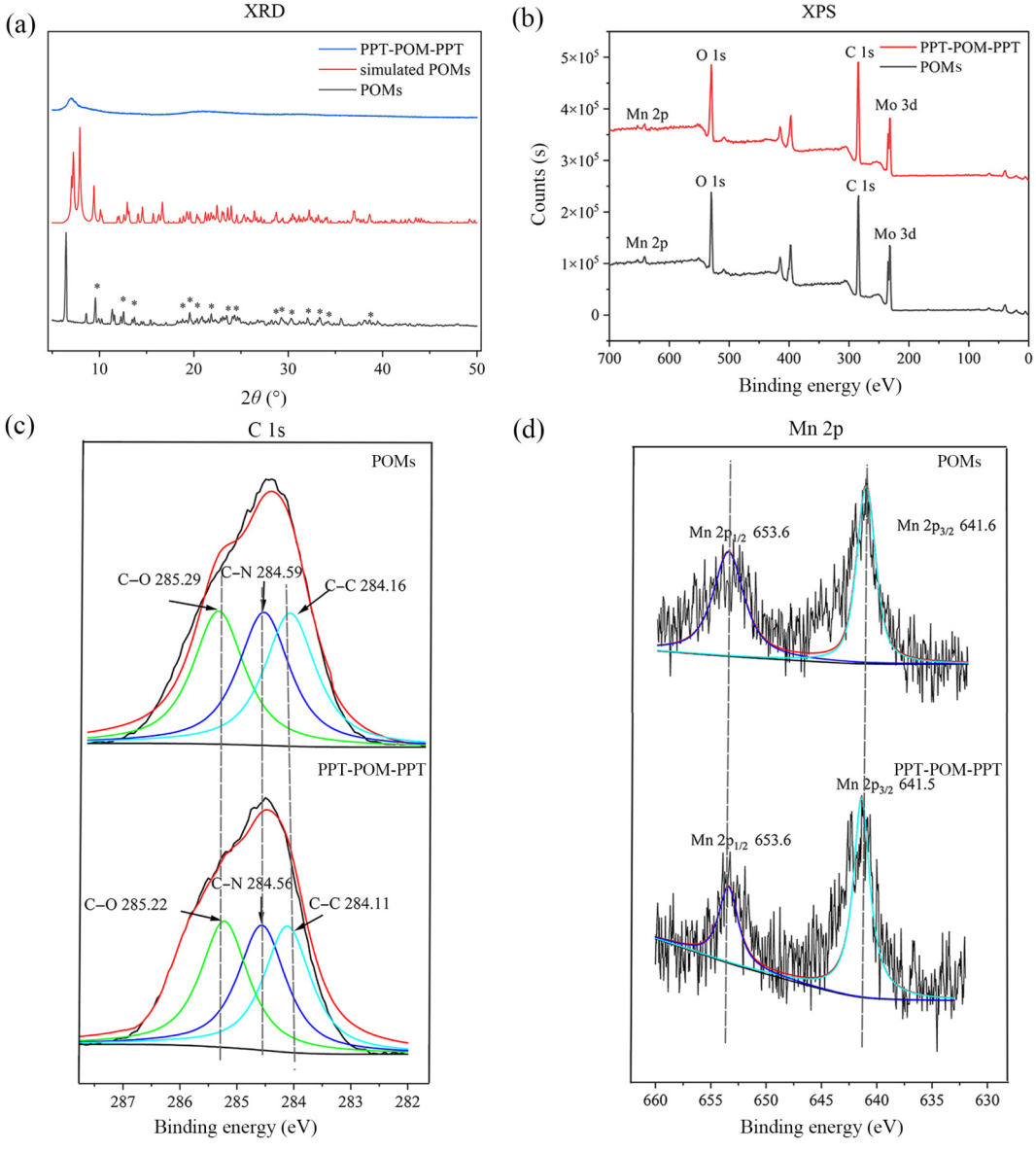

Figure 3 (a) The XRD spectrum of POMs, the simulated XRD spectrum of POMs created using Mercury software, and the XRD spectrum of PPT-POM-PPT. (b) XPS spectra of POMs and PPT-POM-PPT. (c) XPS spectra of C 1s signals for POMs and PPT-POM-PPT. (d) XPS spectra of Mn 2p signals for POMs and PPT-POM-PPT.

spectra of the POMs and PPT-POM-PPT were consistent in terms of the element type and binding energy, which further verified the structural stability of the POMs in PPT-POM-PPT.

3.2 Determination of the CAC

CAC refers to the concentration at which amphiphilic molecules begin to self-assemble to form aggregates [43]. CAC can be measured using several approaches, including physicochemical methods, such as electrical conductivity measurements and fluorescence methods. These methods utilize alterations in the macroscopic parameters to measure the CAC [44]. CAC is primarily used to assess the capability of a compound to form aggregates, indicating it's *in vivo* stability upon dilution [45]. The CAC of the PPT-POM-PPT solution with varying concentrations at five distinct temperatures was determined through conductivity measurements and fluorescence spectrometry.

3.2.1 *Conductivity measurement*

The CAC of the PPT-POM-PPT solution was assessed using the conductivity method (Fig. 4(a)). Electrical conductivity, a measure of the ability of a system to conduct an electric current, increases with increasing molecular concentrations as more number of ions are present per unit volume [46]. The electrical conductivity of amphiphilic molecules, which exist as ions, increased almost linearly with increasing concentrations. However, when the solution concentration reached the CAC, the molecules conducted electricity in the form of aggregates, and the conductivity still increased with concentration, but the change became smaller [47]. When the concentration of PPT-POM-PPT reached 24 μg·mL^{-1}, the linear relationship deviated, and the slope approached a plateau. Therefore, the concentration at this point was the CAC of PPT-POM-PPT. With an increase in temperature, the CAC decreased from 24 to 21 μg·mL^{-1}, indicating that increasing the temperature can help reduce the concentration required to form aggregates by indirectly accelerating aggregate formation. Specifically, high temperatures stimulated more intense thermal motion between molecules, effectively weakening the repulsive effect between molecules. This enables these molecules to attract and aggregate more efficiently, ultimately promoting aggregate formation.

3.2.2 *Fluorescence spectroscopy measurements*

Pyrene is frequently employed as a fluorescent probe to investigate the microdomain formation of amphiphilic molecules in solution. Their unique fluorescence properties, especially the intensity ratio of the first and third emission peaks (I_1/I_3), are used to evaluate the degree of polarity of the microenvironment [48]. The I_1/I_3 ratio changed with varying PPT-POM-PPT concentrations (Fig. 4(b)). At low concentration ranges, the I_1/I_3 value remained at approximately 1.8, similar to the hydrophobic index of pyrene in pure water environments. This suggests that no apparent aggregates were formed within this concentration range. When the concentration exceeded 10 μg·mL^{-1}, the I_1/I_3 value decreased sharply, indicating that PPT-POM-PPT started to form aggregates and dissolve the pyrene. After the second turning point, the I_1/I_3 value remained stable, indicating the formation of almost stable aggregates containing a large number of pyrene molecules. When the concentration exceeded 20 μg·mL^{-1}, the I_1/I_3 values gradually approached the equal state. This confirmed that the CAC of PPT-POM-PPT is 20 μg·mL^{-1}, consistent with the value obtained in the conductivity measurement. The I_1/I_3 values decreased from 1.38 to 1.31 with the increase in temperature, indicating that the aggregates were more closely arranged with the increase in temperature. Increasing the temperature caused the molecules to pack closer together, crowding out more water molecules and reducing the amount of water in the aggregate. Therefore, the I_1/I_3 value of the pyrene molecules decreased in a more hydrophobic environment.

3.3 Characterization of the PPT-POM-PPT vesicles

3.3.1 *Morphology of the PPT-POM-PPT vesicles*

Aggregates are formed when the concentration of the PPT-POM-PPT solution exceeds their CAC. Dynamic light scattering (DLS) analysis showed that the PPT-POM-PPT vesicles (200 μg·mL^{-1}) had an average size of 126 nm and a size distribution or polydispersity index (PDI) of 0.254 (Fig. 5(a)), indicating good dispersibility and a narrow distribution range. Transmission electron microscopy (TEM) images showed that the aggregates were spherical (Figs. 5(c) and 5(d)) with a significant contrast between the center and the periphery, which is characteristic of vesicles [49]. PPT-POM-PPT can self-assemble into hollow spherical vesicles with an average diameter of approximately 100 nm. However, the size obtained from DLS measurements was slightly larger than that from TEM. This might be due to the loss of solvent during the preparation of the samples for TEM. The self-assembling capability of PPT-POM-PPT containing hydrophilic and hydrophobic domains can be attributed to the hydrophobic interactions between the molecules and electrostatic interactions between the POMs [50, 51].

The zeta potential of the PPT-POM-PPT vesicles (200 μg·mL^{-1}) was −30.6 mV. The negative charge indicates that the hydrophilic POMs are located on the outer side of the vesicles, while the

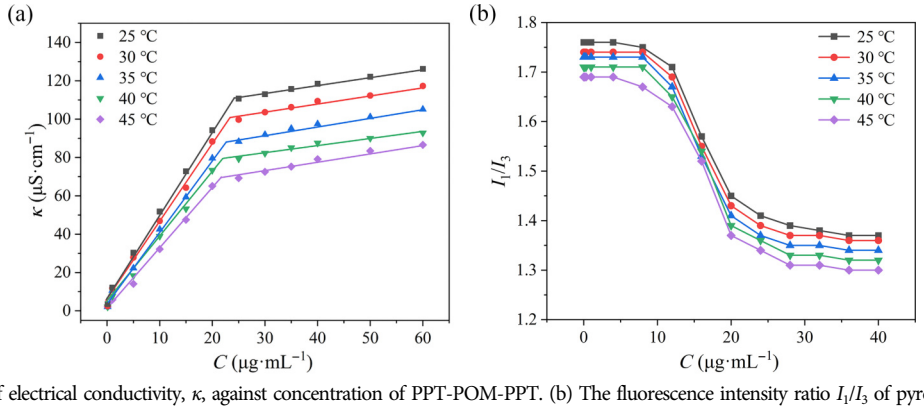

Figure 4 (a) The plots of electrical conductivity, κ, against concentration of PPT-POM-PPT. (b) The fluorescence intensity ratio I_1/I_3 of pyrene as a function of PPT-POM-PPT concentration.

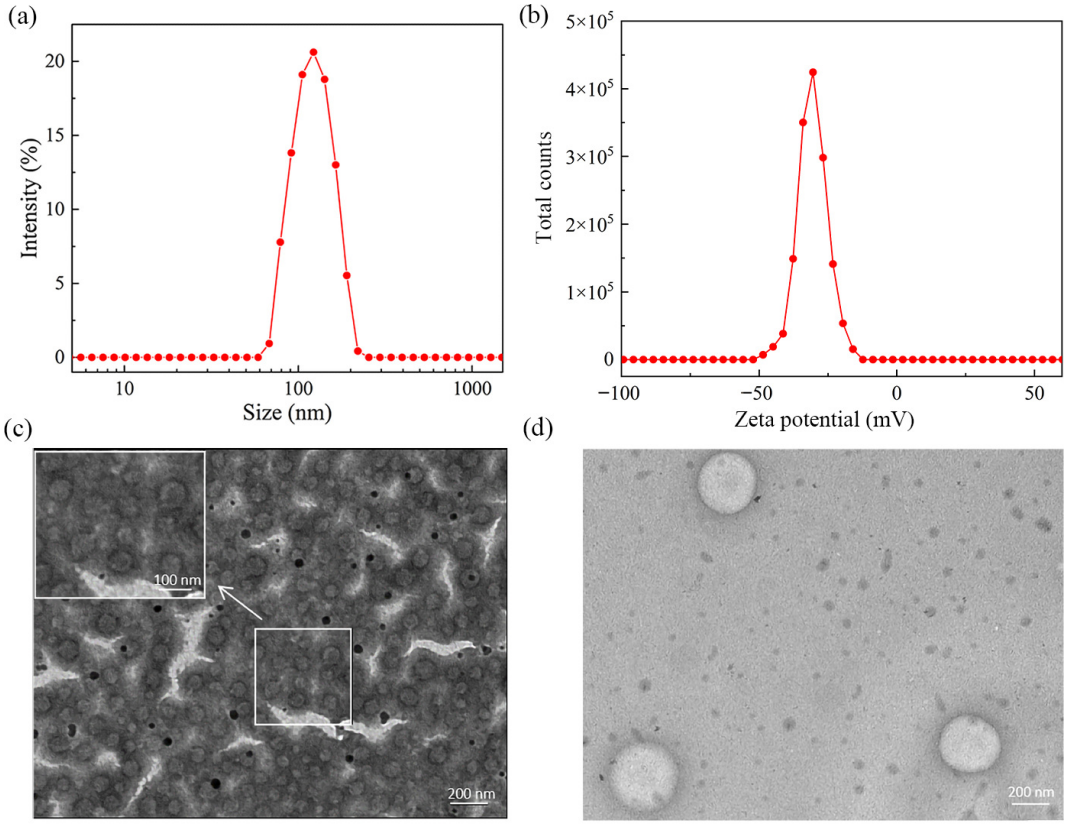

Figure 5 (a) Size distribution of PPT-POM-PPT vesicles measured by DLS (200 μg·mL^{-1}). (b) Zeta potential of PPT-POM-PPT vesicles measured by DLS (200 μg·mL^{-1}). The TEM images of the PPT-POM-PPT vesicles: (c) 200 and (d) 25 μg·mL^{-1}.

hydrophobic PPT face inwards (Fig. 5(b)). The advantage of a negatively charged structure is that it has low interaction with the proteins in the blood after intravenous injection, so it can avoid being cleared by macrophages or the reticuloendothelial system. This, in turn, indicates good stability of the vesicles in the blood circulation [52, 53].

3.3.2 *Stability of the PPT-POM-PPT vesicles*

Maintaining a stable size is a key prerequisite for an effective delivery system [54]. Therefore, the *in vitro* stability of the PPT-POM-PPT vesicles was evaluated by monitoring the size changes. The PPT-POM-PPT vesicles were stored at a constant temperature of 4 °C in the dark for 1, 5, 15, and 30 days. As shown in Figs. 6(a) and 6(b), the sizes of the vesicles remained almost unchanged after 30 days of storage, confirming the remarkable stability of the vesicle system under *in vitro* conditions. Moreover, the low CAC of the vesicles ensures that they maintain their stability and efficiency once they are diluted in the blood after injection. After being diluted 1000 times, the size of the PPT-POM-PPT vesicles remained almost unchanged, maintaining a stable size distribution, with only a slight increase in the PDI value (Fig. 6(c)). These results showed that the PPT-POM-PPT vesicles retain their structure after being diluted to a large extent. In particular, the low concentration at which the vesicles were diluted was not equal to the concentration required for them to self-assemble. In summary, the PPT-POM-PPT vesicles had good dilution stability.

The feasibility of formulating solid preparations using the synthesized vesicles was evaluated using the size and distribution of the lyophilized vesicles as the key performance indicators [55]. The size and PDI of the PPT-POM-PPT vesicles increased slightly after lyophilization, indicating that these vesicles maintain their structural stability upon lyophilization (Figs. 6(d) and 6(e)). Previous studies have shown that the incorporation of specific amounts of cryoprotectants, such as sucrose and mannitol, can significantly enhance the efficacy of lyophilization [56, 57]. Upon adding the cryoprotectant mannitol, the size of the vesicles was almost unchanged, without any increase in PDI. Consequently, adding an appropriate quantity of cryoprotectant to the PPT-POM-PPT vesicles improves their freeze-drying and reconstitution properties, enabling their formulation into solid preparations. These solid preparations exhibited enhanced storage stability over extended periods.

3.3.3 *Hemolysis assay of the PPT-POM-PPT vesicles*

The hemolysis experiments revealed a gradual increase in the hemolysis rate with an increase in the vesicle concentration (Fig. 6(f)). At the maximum concentration of the vesicle solution (200 μg·mL^{-1}), the hemolysis rate was 2.66%, which was within the safe range required by national standards (not exceeding 5%). This indicated that the vesicles had low hemolytic activity and good biocompatibility, making them suitable for intravenous administration without causing adverse effects on the body. Furthermore, the PPT-POM-PPT vesicle solutions exhibited good plasma stability *in vitro* (Fig. S5 in the ESM).

3.4 Cytotoxicity assay of PPT-POM-PPT

The cytotoxicity of PPT-POM-PPT vesicles on the tumor cells H1299, A549, and Hep-G2, and normal hepatocytes HEK293 was evaluated using the MTT assay (Fig. 7). Free PPT showed significant dose-dependent cytotoxicity against all tumor cells and

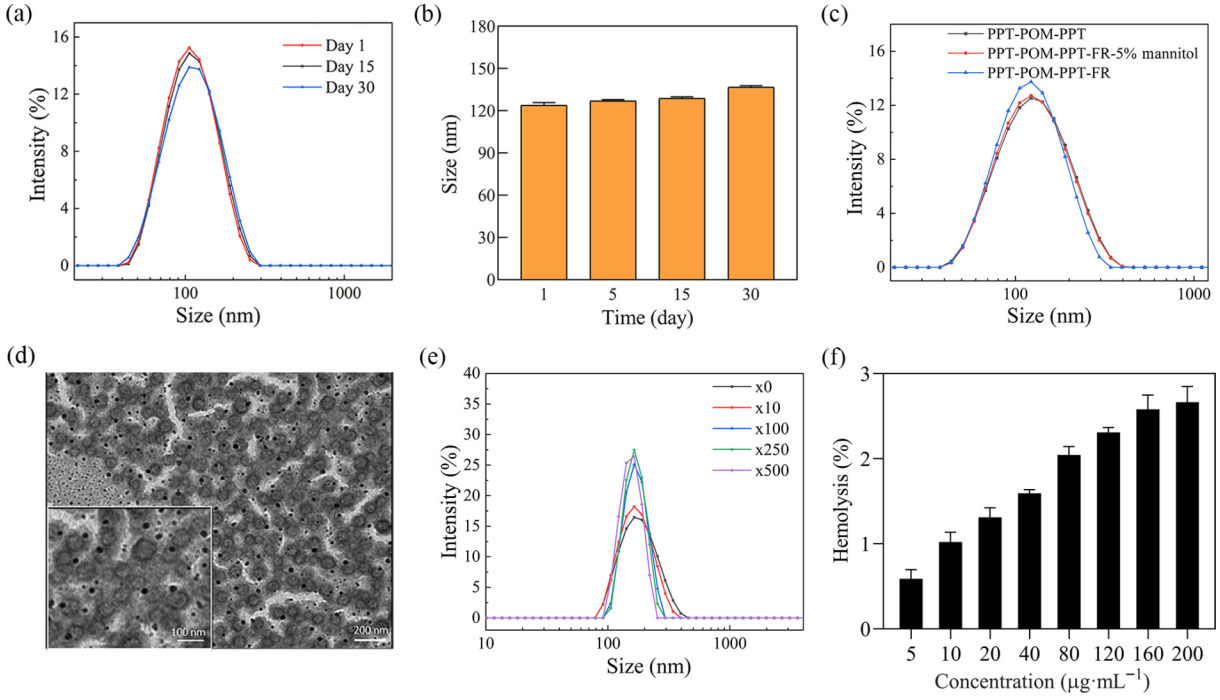

Figure 6 (a) Size distribution of the PPT-POM-PPT vesicle solution at days 1, 15, and 30. (b) Trends in size of PPT-POM-PPT vesicle solutions over a period of 30 days. (c) Comparison of size distribution of PPT-POM-PPT vesicles at different dilutions. (d) TEM images of PPT-POM-PPT vesicles after freeze-dried redissolution. (e) Comparison of freeze-dried redissolution of PPT-POM-PPT vesicles. (f) Hemolysis rates of PPT-POM-PPT at the range of 5 to 200 μg·mL^{-1}. Data presented as mean ± SD, $n = 3$.

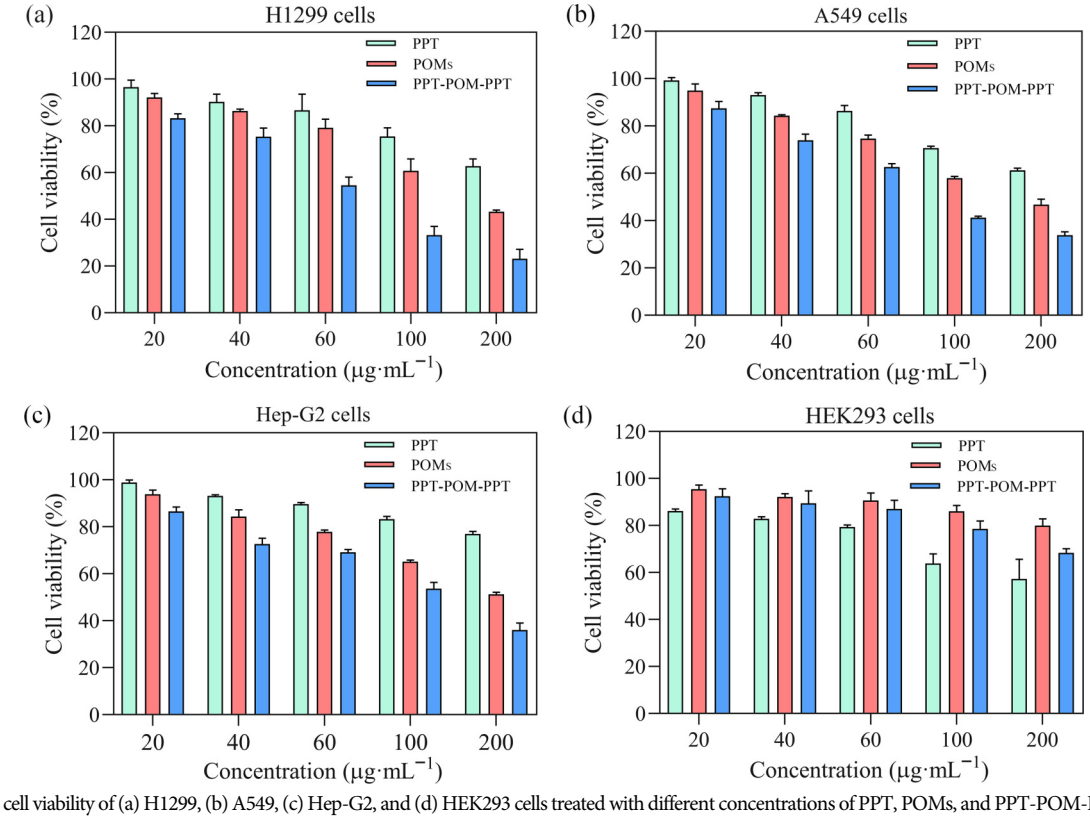

Figure 7 The cell viability of (a) H1299, (b) A549, (c) Hep-G2, and (d) HEK293 cells treated with different concentrations of PPT, POMs, and PPT-POM-PPT for 24 h.

normal HEK293 cell, whereas free POMs were more cytotoxic toward the three cancer cells compared with PPT, with the highest safety against normal HEK293 cells. Notably, the anticancer activity of the PPT-POM-PPT vesicles was significantly enhanced at equivalent PPT and POM concentrations. At 200 μg·mL^{-1}, the PPT-POM-PPT vesicles reduced the activity of A549, Hep-G2, and H1299 cells by 66%, 63%, and 76% respectively. These findings showed the potent inhibitory effects of PPT-POM-PPT vesicles on lung and liver tumor cells, particularly on H1299 tumor cells, whereas the inhibitory effect on normal HEK293 cells was relatively

low. The PPT-POM-PPT vesicles were specifically able to inhibit tumor cell proliferation and were considered safer than free PPT. PPT and POMs also exhibited cytotoxicity toward cancer cells.

After 48 h of incubation, the IC_{50} values of the PPT-POM-PPT vesicles on H1299, A549, and Hep-G2 tumor cells were 60.5, 61.4, and 66.9 μg·mL^{-1}, respectively, which were lower than that for the normal human hepatocytes HEK293 (115.5 μg·mL^{-1}) (Fig. 8 and Table 1). The PPT-POM-PPT vesicles showed dose-dependent and time-dependent cytotoxicity. At 24 h, PPT-POM-PPT showed slightly less cytotoxicity than free PPT on cancer cells. However, when treatment was extended to 48 h, the cytotoxicity of PPT-POM-PPT was significantly more than that of free PPT on cancer cells. Notably, the toxicity of PPT-POM-PPT and free POMs against normal cells decreased slightly when the time was extended from 24 to 48 h, indicating that free POMs and PPT-POM-PPT vesicles were safe for normal cells. The enhanced cytotoxicity of PPT-POM-PPT vesicles emphasized their efficacy as an effective intracellular drug delivery carrier for hydrophobic PPT.

These results were confirmed using the Annexin V-488/PI cell apoptosis assay. Apoptosis-mediated cell death is assessed based on distinct morphological alterations, such as chromatin condensation and DNA fragmentation. The impact of PPT-POM-PPT vesicles on apoptosis was explored using flow cytometry after staining with Annexin V and PI. The quadrants Q1 and Q2 in the upper region indicate necrotic cells (positive for PI) and late-stage apoptotic cells (positive for both PI and Annexin V), respectively, while Q3 in the lower right represents apoptotic cells (positive for annexin). As shown in Fig. 9(b), A549 cells exposed to 100 μg·mL^{-1} of PPT-POM-PPT for 24 h demonstrated an apoptotic rate of 57.19%, significantly higher than that of the untreated control group. Therefore, the PPT-POM-PPT vesicles effectively induce apoptosis in cancer cells.

3.5 Cellular uptake of PPT-POM-PPT

After incubation with PPT-POM-PPT for 1, 3, 6, and 12 h, the green fluorescence intensity increased with time, indicating an increase in the cellular internalization of the vesicles (Figs. 9(c) and 9(d)), which was confirmed by quantitatively analyzing the fluorescence intensity. The green fluorescence signal of the FITC-labeled PPT-POM-PPT vesicle-treated group was significantly higher than that of the control group, irrespective of the incubation time (1, 3, 6, and 12 h). The cellular uptake rate of PPT-POM-PPT by A549 cells was 28.7%. The time-dependent internalization of the vesicles observed using fluorescence microscopy suggested that PPT-

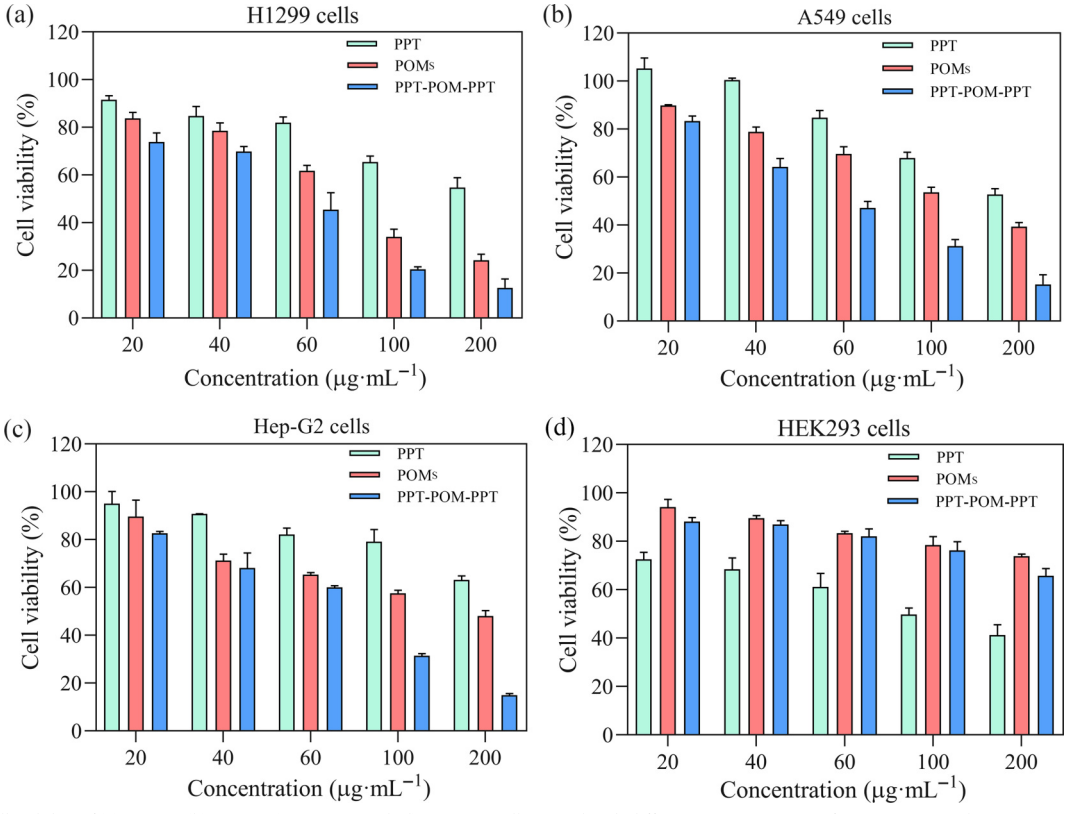

Figure 8 The cell viability of (a) H1299, (b) A549, (c) Hep-G2, and (d) HEK293 cells treated with different concentrations of PPT, POMs, and PPT-POM-PPT for 48 h.

Table 1 IC_{50} values of PPT, POMs and PPT-POM-PPT on H1299, A549, Hep-G2 and HEK293 cells (μg·mL^{-1})

Cell	PPT		POMs		PPT-POM-PPT	
	24 h	48 h	24 h	48 h	24 h	48 h
H1299	311.6	229.3	155.9	78.58	71.5	52.74
A549	266.5	196.2	159.0	126.3	92.41	58.23
Hep-G2	413.4	347.3	199.2	157.1	116.7	66.87
HEK293	273.8	112.7	571.2	447.97	503.5	497.8

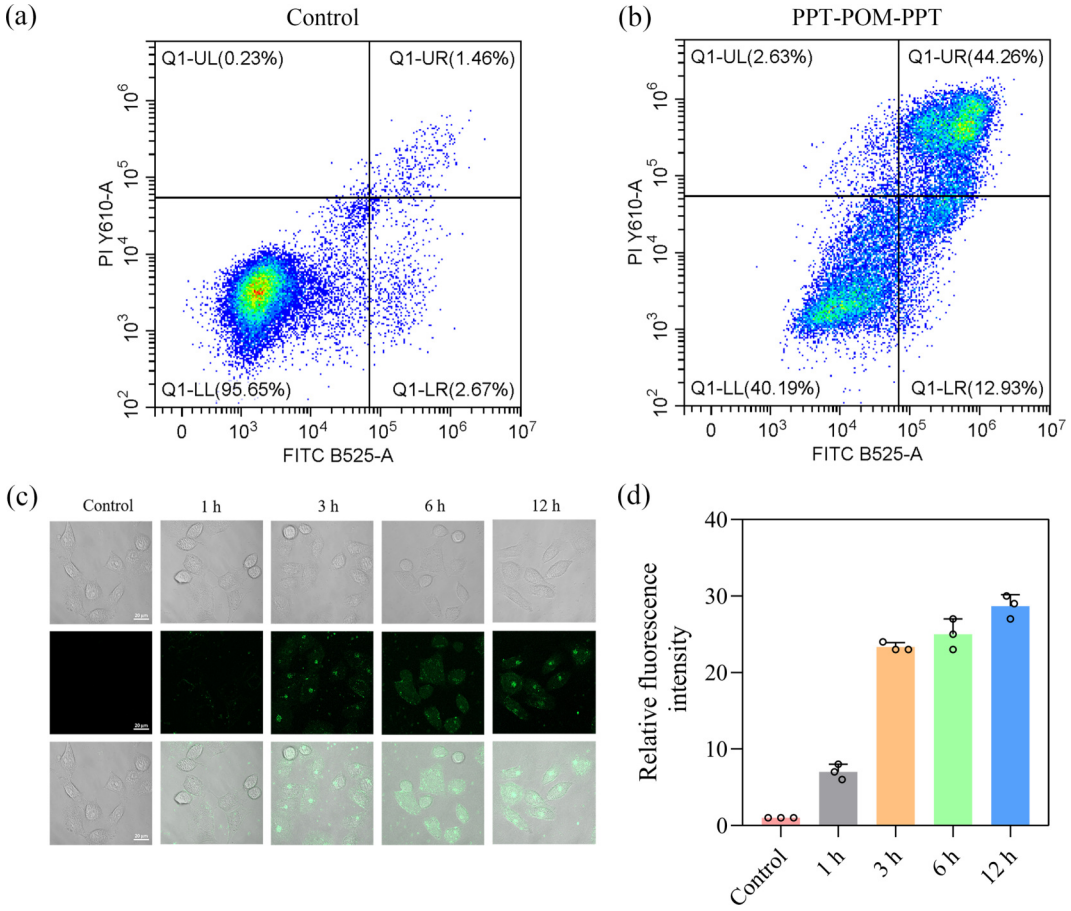

Figure 9 Cell apoptosis and necrosis of A549 cells by flow cytometry: (a) control group and (b) PPT-POM-PPT group. (c) CLSM images of the A549 cells after treatment with FITC-labelled PPT-POM-PPT vesicles for 1, 3 , 6, and 12 h. Scale bars: 20 μm. (d) PPT-POM-PPT vesicles fluorescence intensity of the A549 cells treated as described in (c) determined by Image J software.

POM-PPT possesses enhanced *in vitro* antitumor efficacy.

Fluorescence microscopy was used to observe the PPT-POM-PPT-treated A549 cells. In Fig. 10(a), the experimental groups are shown from left to right: bright-field A549 cells, FITC-labeled PPT-POM-PPT vesicles-treated A549 cells, and the merged images of both. Control A549 cells were non-fluorescent. After incubation with FITC-labeled PPT-POM-PPT vesicles, the A549 cells exhibited green fluorescence, indicating the successful loading of FITC into the PPT-POM-PPT vesicles.

The cellular uptake of FITC-labeled PPT-POM-PPT vesicles was observed with CLSM using A549 cells cultured with Lyso-Tracker Red, a red dye used to label lysozymes, for 8 h (Fig. 10(b)). CLSM images showed that the A549 cells incubated with the FITC-labeled PPT-POM-PPT vesicles for 8 h exhibited green fluorescence. In the merged images, the red fluorescence of the lysosomes overlapped with the green fluorescence of the PPT-POM-PPT vesicles, presenting mixed colors of red and green. This indicated that the FITC signals were co-localized with the tumor cells. Moreover, as shown by the numerical results of the fluorescence intensity, the uptake of the PPT-POM-PPT vesicles by A549 cells was higher than that of the control. Moreover, the FITC-labeled PPT-POM-PPT localized in the lysosomes within the A549 cells, indicated that these vesicles might exert their inhibitory effect via the lysosomal pathway, making them promising candidates for anticancer drug applications.

As shown in the TEM images, the synthesized amphiphilic drug PPT-POM-PPT could self-assemble into hollow spherical vesicles in aqueous solutions. Intermolecular hydrophobic and electrostatic interactions between POMs were the main driving forces for the self-assembly of the PPT-POM-PPT vesicles. The zeta potential confirmed the presence of a negative charge, indicating the structural characteristics of the vesicles. Based on this, the hydrophilic POM ends are oriented toward the periphery, while the hydrophobic PPT ends are preferentially located within the interior of the vesicles. The relatively low CAC value shows the high stability of PPT-POM-PPT in aqueous solutions. Although the hemolysis rate was shown to rise gradually with increasing vesicle concentrations, this rate remained within the acceptable safety limits. These results prove that the vesicles are highly safe, with low hemolytic toxicity and good biocompatibility. The MTT assay showed that the PPT-POM-PPT vesicles showed stronger anticancer activity against H1299, A549, and Hep-G2 tumor cells but showed relatively lower cytotoxicity against HEK293 normal cells. Compared with free PPT, PPT-POM-PPT vesicles were safer toward normal cells while showing significantly higher inhibitory effects on cancer cells. The CLSM observations confirmed the effective uptake of the PPT-POM-PPT vesicles by tumor cells and their co-localization with lysosomes. Therefore, the vesicles were successfully transported within the cell and could be effectively released. Existing studies suggest that POMs exert their anticancer effects by inhibiting adenosine triphosphate synthesis, interfering with electron transfer, increasing ROS, accelerating glutathione

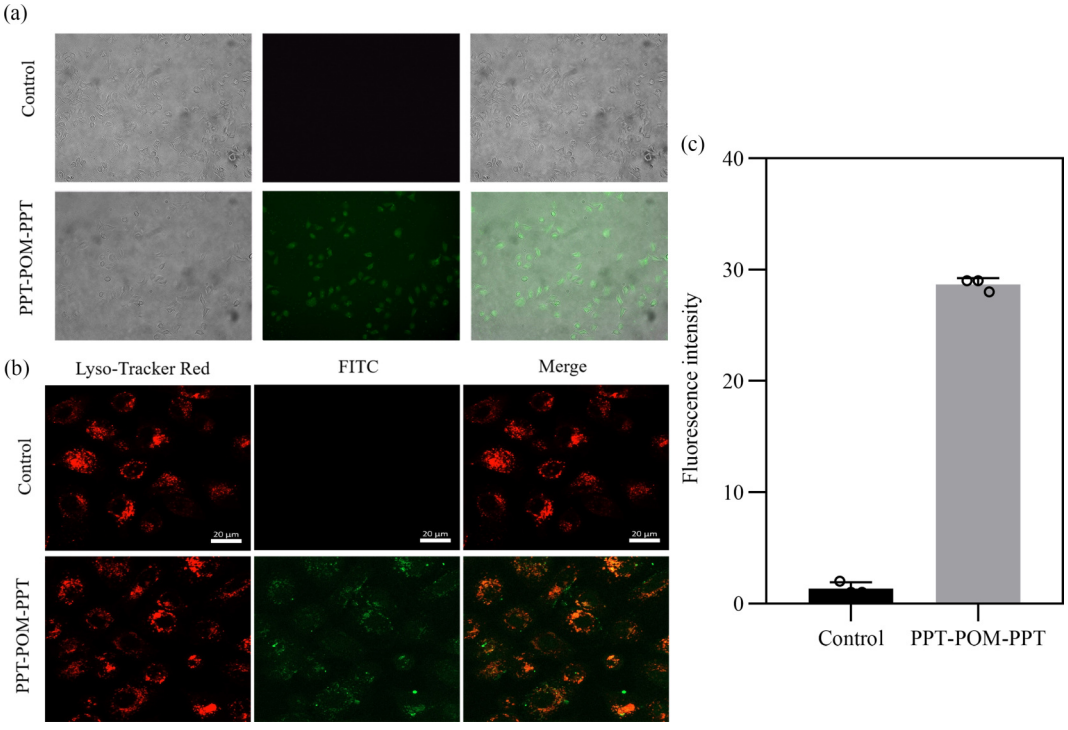

Figure 10 (a) Fluorescence microscope observation of A549 cells after treatment with PPT-POM-PPT vesicles. (b) CLSM images of the A549 cells treated with PPT-POM-PPT vesicles for 8 h. Scale bars: 20 μm. (c) PPT-POM-PPT vesicles fluorescence intensity of the A549 cells treated as described in (a) determined by Image J software.

consumption, directly inducing DNA damage, and promoting cell apoptosis [58, 59]. These current results suggested that the enhanced anti-cancer efficacy of the PPT-POM-PPT vesicles can be attributed to a mechanism similar to that of POMs. The synthesis of PPT-POM-PPT vesicles highlighted the potential and application of POMs drugs in antitumor therapy, providing a novel approach to cancer treatment.

4 Conclusion

POMs can inhibit the growth of various tumors, but their applications as anti-tumor agents are limited due to their low lipid solubility and higher dose requirements. To overcome these drawbacks, the hydrophobic anticancer drug PPT was covalently modified with hydrophilic POMs in organic groups, significantly enhancing its anticancer activity. The prepared amphiphilic drug PPT-POM-PPT can self-assemble into vesicles in aqueous solutions. TEM and zeta potential analyses revealed that these vesicles were negatively charged hollow spherical structures, with a hydrophilic POM terminal on the periphery and a hydrophobic PPT terminal on the interior. Their low CAC values attested to their high stability, while the hemolysis test results showed good compatibility with blood. MTT assays revealed that the PPT-POM-PPT vesicles had good anti-cancer activity against H1299, A549, and Hep-G2 tumor cells while exhibiting lower toxicity toward HEK293 normal cells. Therefore, these PPT-POM-PPT vesicles can significantly enhance cancer cell inhibition while ensuring safety toward normal cells, achieving a synergistic effect. CLSM imaging revealed their effective intracellular uptake and co-localization with lysosomes, suggesting a potential lysosomal drug delivery and release pathway. Our findings provide valuable insights for the application of these vesicles in anti-tumor therapy.

These novel PPT-POM-PPT vesicles effectively deliver drugs without requiring additional carrier materials, which improves drug stability and biocompatibility. Moreover, they integrate the anti-tumor effects of PPT and POMs. These vesicles are effectively taken up by tumor cells, inhibiting their growth. This dual mechanism of action makes these POMs promising candidates for tumor therapy, laying a theoretical foundation for their future clinical applications and uncovering new therapeutic avenues. Furthermore, the successful development of the PPT-POM-PPT vesicles underscores the potential and broad application prospects of POM drugs in treating multiple diseases.

Electronic Supplementary Material: Supplementary material (^{1}H NMR spectra of PPT and POMs; EMI-MS spectra of POMs and PPT-POM-PPT; plasma stability of PPT-POM-PPT vesicles) is available in the online version of this article at https://doi.org/10.26599/POM.2025.9140085.

Data availability

All data needed to support the conclusions in the paper arepresented in the manuscript and the Electronic Supplementary Material.

Acknowledgements

This work was supported by the Natural Science Foundation of China (No. 21801153), Natural Science Foundation of Shandong Province (No. ZR2023MB065), the Shandong Province Chinese Medicine Science and Technology Development Project (No. M-2022258), Young Scientist Development Foundation of Shandong First Medical University (No. 202201-002), and the Academic Promotion Program of Shandong First Medical University (No. 2019LJ003).

Declaration of competing interest

The authors have no competing interests to declare that are relevant to the content of this article.

Author contribution statement

L. M. L.: Investigation, writing – original draft. Y. X. S.: Writing – original draft. J. Y. L.: Data curation, methodology. Q. F. W.: Investigation, conceptualization. J. C. W.: Methodology. X. C. L.: Investigation. D. J. Z.: Writing – review & editing, methodology. T. L.: Supervision, writing – review & editing.

Informed consent

Not applicable.

Ethics statement

Not applicable.

Use of AI statement

None.

References

[1] Liu, Q. D.; Zhang, Q. H.; Shi, W. X.; Hu, H. S.; Zhuang, J.; Wang, X. Self-assembly of polyoxometalate clusters into two-dimensional clusterphene structures featuring hexagonal pores. *Nat. Chem.* **2022**, *14*, 433–440.

[2] Yu, C. Z.; Hu, Y.; Yang, J. L.; Huang, J. S.; Li, B.; Wu, L. X.; Li, F. H. Efficient and stable inverted perovskite solar cells with $TOASiW_{12}$-modified AI as a cathode. *Adv. Funct. Mater.* **2023**, *33*, 2209290.

[3] Li, K.; Liu, Y. F.; Yang, G. P.; Zheng, Z. L.; Lin, X. L.; Zhang, Z. B.; Li, S. J.; Liu, Y. H.; Wei, Y. G. Highly-stable silverton-type U^{IV}-containing polyoxomolybdate frameworks for the heterogeneous catalytic synthesis of quinazolinones. *Green Chem.* **2024**, *26*, 6454–6460.

[4] Huang, X. Q.; Liu, S.; Liu, G.; Tao, Y. W.; Wang, C. R.; Zhang, Y. L.; Li, Z.; Wang, H. W.; Zhou, Z.; Shen, G. D. et al. An unprecedented 2-fold interpenetrated *lvt* open framework built from Zn_6 ring seamed trivacant polyoxotungstates used for photocatalytic synthesis of pyridine derivatives. *Appl. Catal. B: Environ.* **2023**, *323*, 122134.

[5] Zhang, H. Y.; Zhao, W. L.; Li, H. Q.; Zhuang, Q. H.; Sun, Z. Q.; Cui, D. Y.; Chen, X. J.; Guo, A.; Ji, X.; An, S. et al. Latest progress in covalently modified polyoxometalates-based molecular assemblies and advanced materials. *Polyoxometalates* **2022**, *1*, 9140011.

[6] Aureliano, M.; Gumerova, N. I.; Sciortino, G.; Garribba, E.; Rompel, A.; Crans, D. C. Polyoxovanadates with emerging biomedical activities. *Coord. Chem. Rev.* **2021**, *447*, 214143.

[7] Shi, Y. H.; Zhang, J. J.; Huang, H.; Cao, C. Y.; Yin, J. J.; Xu, W. J.; Wang, W. J.; Song, X. J.; Zhang, Y. W.; Dong, X. C. Fe-doped polyoxometalate as acid-aggregated nanoplatform for NIR-II photothermal-enhanced chemodynamic therapy. *Adv. Healthc. Mater.* **2020**, *9*, 2000005.

[8] Cheng, Y.; Qin, K. J.; Zang, D. J. Polyoxometalates based nanocomposites for bioapplications. *Rare Met.* **2023**, *42*, 3570–3600.

[9] Garrido Ribó, E.; Bell, N. L.; Xuan, W. M.; Luo, J. C.; Long, D. L.; Liu, T. B.; Cronin, L. Synthesis, assembly, and sizing of neutral, lanthanide substituted molybdenum blue wheels $\{Mo_{90}Ln_{10}\}$. *J. Am. Chem. Soc.* **2020**, *142*, 17508–17514.

[10] Hu, Q. L.; Liu, Y. F.; Lin, X. L.; Lin, Z. F.; Cao, J. W.; Yang, G. P. Two different three-dimensional uranium-containing polymolybdates based on Zn(II) for the heterogeneous catalytic construction of C–N bond. *Inorg. Chem.* **2024**, *63*, 8919–8924.

[11] Xu, T. T.; Li, Y. W.; Wei, Z. Z.; Liu, S.; Sun, J. N.; Jin, R. C.; Song, Y. B. Controllable self-assembly of atomically precise $Au_{31}Cu_{32}$ nanoclusters into superstructures. *Mater. Today Chem.* **2024**, *36*, 101922.

[12] Li, S. L.; Zhang, S. S.; Feng, N.; Zhang, N.; Zhu, Y.; Liu, Y. H.; Wang, W. J.; Xin, X. Chiral inversion and recovery of supramolecular luminescent copper nanocluster hydrogels triggered by polyethyleneimine and polyoxometalates. *ACS Appl. Mater. Interfaces* **2022**, *14*, 52324–52333.

[13] Salazar Marcano, D. E.; Lentink, S.; Chen, J. J.; Anyushin, A. V.; Moussawi, M. A.; Bustos, J.; Van Meerbeek, B.; Nyman, M.; Parac-Vogt, T. N. Supramolecular self-assembly of proteins promoted by hybrid polyoxometalates. *Small* **2024**, *20*, 2312009.

[14] Huo, Z. H.; Liang, Y. M.; Lv, Y. K.; Melin, F.; Hellwig, P.; Ibrahim, H.; Goldmann, M.; Boudon, C.; Badets, V.; Bonnefont, A. et al. Enhancement of photocurrent by incorporation of preyssler type polyoxometalate protected nanoparticles in polyporphyrin films. *Chem. Commun.* **2021**, *57*, 1482–1485.

[15] Xiao, H. P.; Hao, Y. S.; Li, X. X.; Xu, P.; Huang, M. D.; Zheng, S. T. A water-soluble antimony-rich polyoxometalate with broad-spectrum antitumor activities. *Angew. Chem., Int. Ed.* **2022**, *61*, e202210019.

[16] Qu, X. S.; Shi, D.; Fu, Y.; Chu, D. X.; Yang, Y. Y.; Liu, Y. Enhanced antitumor activity of polyoxometalates loaded solid lipid nanoparticles. *Inorg. Chem. Commun.* **2021**, *124*, 108411.

[17] Dolbecq, A.; Dumas, E.; Mayer, C. R.; Mialane, P. Hybrid organic-inorganic polyoxometalate compounds: From structural diversity to applications. *Chem. Rev.* **2010**, *110*, 6009–6048.

[18] Liu, G.; Chen, Y. F.; Chen, Y. L.; Shi, Y. Q.; Zhang, M. Y.; Shen, G. D.; Qi, P. F.; Li, J. K.; Ma, D. L.; Yu, F. et al. Indirect electrocatalysis S–N/S–S bond construction by robust polyoxometalate based foams. *Adv. Mater.* **2023**, *35*, 2304716.

[19] Wang, Z. C.; Zhang, S. S.; Xie, H. Y.; Zhang, N.; Wang, W. J.; Li, S. L.; Xin, X. Dispersing hydrophobic copper nanoclusters in aqueous solutions triggered by polyoxometalate with aggregation-induced eimission properties. *Colloids Surf. A: Physicochem. Eng. Asp.* **2023**, *664*, 131147.

[20] Chen, K.; Liu, S. Q.; Wei, Y. J. Sub-nanosized vanadate hybrid clusters maintain glucose homeostasis and restore treatment response in inflammatory disease in obese mice. *Nano Res.* **2024**, *17*, 1818–1826.

[21] Xia, Z. Q.; Yang, Y.; Song, Y. F.; Shi, S. W. Self-assembly of polyoxometalate-based nanoparticle surfactants in solutions. *ACS Macro Lett.* **2024**, *13*, 99–104.

[22] Huang, S.; Jin, Q.; Wang, Y.; Sun, Y. H.; Wang, F. Z. RETRACTED: Anti-liver cancer activity evaluation of a polyoxometalate-organic co-crystal compound and its related coordination polymer. *Main Group Chem.* **2019**, *18*, 231–238.

[23] Liu, C.; Cheng, Z.; Xu, X. D.; Wang, N.; Luo, X. W.; Xin, X. Fluorescent nanocomposite prepared through supramolecular self-assembly of a tetraphenylethene derivative and polyoxometalate for light-emitting diodes. *ACS Appl. Nano Mater.* **2024**, *7*, 11455–11464.

[24] She, S.; Bian, S. T.; Hao, J.; Zhang, J. W.; Zhang, J.; Wei, Y. G. Aliphatic organoimido derivatives of polyoxometalates containing a bioactive ligand. *Chem.—Eur. J.* **2014**, *20*, 16987–16994.

[25] Wang, X. H.; Liu, J. F.; Li, J. X.; Yang, Y.; Liu, J. T.; Li, B.; Pope, M. T. Synthesis and antitumor activity of cyclopentadienyltitanium substituted polyoxotungstate $[CoW_{11}O_{39}(CpTi)]^{7-}$ (Cp = η^5-C_5H_5). *J. Inorg. Biochem.* **2003**, *94*, 279–284.

[26] Yang, H. K.; Cheng, Y. X.; Su, M. M.; Xiao, Y.; Hu, M. B.; Wang,

W.; Wang, Q. Polyoxometalate-biomolecule conjugates: A new approach to create hybrid drugs for cancer therapeutics. *Bioorg. Med. Chem. Lett.* **2013**, *23*, 1462–1466.

[27] Ding, J. H.; Liu, Y. F.; Tian, Z. T.; Lin, P. J.; Yang, F.; Li, K.; Yang, G. P.; Wei, Y. G. Uranyl-silicotungstate-containing hybrid building units {α-SiW_9} and {γ-SiW_{10}} with excellent catalytic activities in the three-component synthesis of dihydropyrimidin-2(1*H*)-ones. *Inorg. Chem. Front.* **2023**, *10*, 3195–3201.

[28] Chen, K.; Qin, Y. R.; Liu, S. Q.; Chen, R. L. Remission of iron overload in adipose tissue of obese mice by fatty acid-modified polyoxovanadates. *Rare Met.* **2025**, *44*, 461–471.

[29] Cheng, X. H.; Sun, P. P.; Zhang, S. S.; Sun, D.; Jiang, B. L.; Wang, W. S.; Xin, X. Self-assembly of m-phenylenediamine and polyoxometalate into hollow-sphere and core-in-hollow-shell nanostructures for selective adsorption of dyes. *J. Mol. Liq.* **2019**, *287*, 110982.

[30] Li, X.; Pillai, S. C.; Wei, L.; Liu, Z. Z.; Huang, L. X.; Huang, Q.; Jia, X. S.; Hou, D. Y.; Song, H.; Wang, H. L. Facile synthesis of polyoxometalate-modified metal organic frameworks for eliminating tetrabromobisphenol-A from water. *J. Hazard. Mater.* **2020**, *399*, 122946.

[31] Hu, H. F.; Pang, J. J.; Gong, P. J.; Chen, L. J.; Zhao, J. W. Organic-inorganic two-dimensional hybrid networks constructed from pyridine-4-carboxylate-decorated organotin-lanthanide heterometallic antimotungstates. *Inorg. Chem.* **2020**, *59*, 11287–11297.

[32] Zhou, Q. P.; Jiang, X. Y.; Zhang, X. C.; Wang, D. W.; Yang, G.; Zhou, H.; Wu, Y. C.; Guo, F.; Chen, M.; Diao, G. W. et al. Polyoxomolybdate-based metal-organic framework-derived Cu-embedded molybdenum dioxide hybrid nanoparticles as highly efficient electrocatalysts for Al–S batteries. *ChemSusChem* **2024**, *17*, e202400424.

[33] Yang, H. K.; Yang, K. M.; Zhang, Z. Y. Self-assembly of polyoxometalate-based hybrid molecules into nanoparticles or vesicles regulated by simple experimental manipulation. *Colloid Polym. Sci.* **2019**, *297*, 957–965.

[34] Fu, L.; Gao, H. Q.; Yan, M.; Li, S. Z.; Li, X. Y.; Dai, Z. F.; Liu, S. Q. Polyoxometalate-based organic-inorganic hybrids as antitumor drugs. *Small* **2015**, *11*, 2938–2945.

[35] Hasenknopf, B.; Delmont, R.; Herson, P.; Gouzerh, P. Anderson-type heteropolymolybdates containing Tris(alkoxo) ligands: Synthesis and structural characterization. *Eur. J. Inorg. Chem.* **2002**, *2002*, 1081–1087.

[36] Marcoux, P. R.; Hasenknopf, B.; Vaissermann, J.; Gouzerh, P. Developing remote metal binding sites in heteropolymolybdates. *Eur. J. Inorg. Chem.* **2003**, *2003*, 2406–2412.

[37] Ling, L. B.; Yao, C.; Du, Y. W.; Ismail, M.; He, R. Y.; Hou, Y. P.; Zhang, Y.; Li, X. S. Assembled liposomes of dual podophyllotoxin phospholipid: Preparation, characterization and *in vivo* anticancer activity. *Nanomedicine* **2017**, *12*, 657–672.

[38] Zhao, W.; Cong, Y.; Li, H. M.; Li, S. Y.; Shen, Y. M.; Qi, Q. S.; Zhang, Y. M.; Li, Y. Z.; Tang, Y. J. Challenges and potential for improving the druggability of podophyllotoxin-derived drugs in cancer chemotherapy. *Nat. Prod. Rep.* **2021**, *38*, 470–488.

[39] Ramezani Aliakbari, M.; Varshosaz, J.; Sadeghi-Aliabadi, H.; Hassanzadeh, F.; Rostami, M. Biotin-targeted nanomicellar formulation of an anderson-type polyoxomolybdate: Synthesis and *in vitro* cytotoxicity evaluations. *Langmuir* **2021**, *37*, 6475–6489.

[40] Blazevic, A.; Rompel, A. The Anderson-Evans polyoxometalate: From inorganic building blocks via hybrid organic-inorganic structures to tomorrows "Bio-POM". *Coord. Chem. Rev.* **2016**, *307*, 42–64.

[41] Zhang, Q. Y.; Lei, D. D.; Luo, Q. Z.; Wang, J. L.; Deng, T. L.; Zhang, Y. T.; Ma, P. H. Efficient biodiesel production from oleic acid using metal-organic framework encapsulated Zr-doped polyoxometalate nano-hybrids. *RSC Adv.* **2020**, *10*, 8766–8772.

[42] Martin, C.; Lamonier, C.; Fournier, M.; Mentré, O.; Harlé, V.; Guillaume, D.; Payen, E. Preparation and characterization of 6-molybdocobaltate and 6-molybdoaluminate cobalt salts. Evidence of a new heteropolymolybdate structure. *Inorg. Chem.* **2004**, *43*, 4636–4644.

[43] Narayan Yadav, S.; Rai, S.; Shah, P.; Roy, N.; Bhattarai, A. Spectrophotometric and conductometric studies on the interaction of surfactant with polyelectrolyte in the presence of dye in aqueous medium. *J. Mol. Liq.* **2022**, *355*, 118949.

[44] Dai, L. X.; Wang, T.; Liu, Y. T.; Lan, Y. J.; Ji, L.; Jiang, J. X.; Li, P. F. Fluorescence probe technique for determining the hydrophobic interactions and critical aggregation concentrations of *Gleditsia microphylla* gum, circular *Gleditsia sinensis* gum, and tara gum. *Int. J. Biol. Macromol.* **2023**, *247*, 125707.

[45] Schmid, P.; Buchecker, T.; Khoshsima, A.; Touraud, D.; Diat, O.; Kunz, W.; Pfitzner, A.; Bauduin, P. Self-assembly of a short amphiphile in water controlled by superchaotropic polyoxometalates: $H_4SiW_{12}O_{40}$ vs. $H_3PW_{12}O_{40}$. *J. Colloid Interface Sci.* **2021**, *587*, 347–357.

[46] Tiwari, S.; Mall, C.; Solanki, P. P. CMC studies of CTAB, SLS & tween 80 by spectral and conductivity methodology to explore its potential in photogalvanic cell. *Surf. Interfaces* **2020**, *18*, 100427.

[47] Niraula, T. P.; Shah, R.; Kumar, D.; Dominguez, H.; Ríos-López, M.; Salazar-Arriaga, A. B.; De, R.; Bhattarai, A. Influence of solvent permittivity and divalent salt on micellization behavior of sodium dodecyl sulfate: Conductivity measurements and simulation study. *J. Mol. Liq.* **2022**, *349*, 118186.

[48] Wu, R. L. G.; Tian, M. C.; Shu, C.; Zhou, C. C.; Guan, W. J. Determination of the critical micelle concentration of surfactants using fluorescence strategies. *Soft Matter.* **2022**, *18*, 8920–8930.

[49] Wang, P.; Wang, Z. T.; Wang, P. S.; Chishti, A. N.; Zhang, H. X.; Shi, J. H.; Ni, L. B.; Jamil, S.; Wei, Y. G. Supramolecular self-assembly of polyoxometalates and cyclodextrin: Progress and perspectives. *Polyoxometalates* **2024**, *3*, 9140047.

[50] Chu, Y.; Saad, A.; Yin, P. C.; Wu, J. Y. Z.; Oms, O.; Dolbecq, A.; Mialane, P.; Liu, T. B. Light-and solvent-controlled self-assembly behavior of spiropyran-polyoxometalate-alkyl hybrid molecules. *Chem.—Eur. J.* **2016**, *22*, 11756–11762.

[51] Zhang, Y. W.; Wang, J. Q.; Chen, Z.; Xie, Y. P.; Wu, J. Q.; Wang, X. J.; Zang, D. J.; Liu, T. Polyoxometalates-based vesicles for application in biological systems. *Mater. Today Commun.* **2022**, *33*, 104991.

[52] Fang, D. X.; Pi, M. H.; Pan, Z. C.; Song, N. J.; He, X. L.; Li, J. H.; Luo, F.; Tan, H.; Li, Z. Stable, bioresponsive, and macrophage-evading polyurethane micelles containing an anionic tripeptide chain extender. *ACS Omega* **2019**, *4*, 16551–16563.

[53] Traldi, F.; Liu, P. F.; Albino, I.; Ferreira, L.; Zarbakhsh, A.; Resmini, M. Protein-nanoparticle interactions govern the interfacial behavior of polymeric nanogels: Study of protein corona formation at the air/water interface. *Int. J. Mol. Sci.* **2023**, *24*, 2810.

[54] Zhao, L. S.; Ckurshumova, W.; Fefer, M.; Liu, J.; Hoare, T. Fabrication, characterization and *in planta* uptake of engineered surfactant nanovesicles for the delivery of the biostimulant sodium copper chlorophyllin. *J. Agric. Food Chem.* **2022**, *70*, 15028–15037.

[55] Moataz El-Dahmy, R.; Hassen Elshafeey, A.; Ahmed El-Feky, Y. Fabrication, optimization, and evaluation of lyophilized lacidipine-loaded fatty-based nanovesicles as orally fast disintegrating sponge delivery system. *Int. J. Pharm.* **2024**, *655*, 124035.

[56] Zhang, T. Y.; Zheng, X. X.; Lin, R. Y.; Sun, H.; Wu, H. H.; Zhang, J. S.; Chen, S. H.; Li, Y. S.; Xu, D. H.; Gao, J. Q. Lyophilizable stem cell-hybrid liposome with long-term stability and high targeting

capacity. *Adv. Healthc. Mater.* **2024**, *13*, 2400704.
[57] Meulewaeter, S.; Nuytten, G.; Cheng, M. H. Y.; De Smedt, S. C.; Cullis, P. R.; De Beer, T.; Lentacker, I.; Verbeke, R. Continuous freeze-drying of messenger RNA lipid nanoparticles enables storage at higher temperatures. *J. Control. Release* **2023**, *357*, 149–160.
[58] Fan, X. F.; Pang, W.; Feng, H.; Zhang, R. Y.; Zhu, W. T.; Wang, Q. S.; Miao, J.; Li, Y. W.; Liu, Y. J.; Xu, X. Q. Light-guided tumor diagnosis and therapeutics: From nanoclusters to polyoxometalates. *Chin. Chem. Lett.* **2022**, *33*, 2783–2798.
[59] Bijelic, A.; Aureliano, M.; Rompel, A. Polyoxometalates as potential next-generation metallodrugs in the combat against cancer. *Angew. Chem., Int. Ed.* **2019**, *58*, 2980–2999.

Lingmei Li is studying for master's degree in Shandong First Medical University & Shandong Academy of Medical Sciences, China. She is working on the design and organic modification of polyoxometalates.

Dejin Zang obtained his Ph.D. degree from University of Strasbourg in 2017. He is working as an associate professor at Shandong First Medical University & Shandong Academy of Medical Sciences, China. He is exploring the preparation of polyoxometalate complexes and their application in electrocatalytic organocatalytic reactions.

Teng Liu obtained her Ph.D. degree from Shandong University in China in 2013. She has been working at Shandong First Medical University & Shandong Academy of Medical Sciences, China. Her research interests are the structural design and mechanism of polyoxometalates, the design of functional drug molecules of polyoxometalates.

Open Access This article is licensed under the terms of the Creative Commons Attribution 4.0 International License (http://creativecommons.org/licenses/by/4.0/), which permits use, sharing, distribution and reproduction in any medium, provided the original work is properly cited.

© The author(s) 2025. Published by Tsinghua University Press.